ACS APPLIED MATERIALS & INTERFACES

Research Article

www.acsami.org

Highly Uniform Hollow GdF_3 Spheres: Controllable Synthesis, Tuned Luminescence, and Drug-Release Properties

Ruichan Lv, Shili Gai,* Yunlu Dai, Na Niu, Fei He, and Piaoping Yang*

Key Laboratory of Superlight Materials and Surface Technology, Ministry of Education, Harbin Engineering University, Harbin 150001, People's Republic of China

Supporting Information

ABSTRACT: In this paper, uniform hollow mesoporous GdF_3 micro/nanospheres were successfully prepared by a facile two-step synthesis route without using any surfactant, catalyst, and further calcination process. The precursor $Gd(OH)CO_3$ spheres are prepared by a coprecipitation process. After that, uniform and size-tunable GdF_3 hollow spheres were easily coprecipitated with $NaBF_4$ at the sacrifice of the precursor with low temperature and short reaction time. X-ray diffraction, scanning electron microscopy, transmission electron microscopy, high-resolution TEM, N_2 adsorption/desorption, and up-conversion (UC) photoluminescence spectra were used to characterize the as-obtained products. It is found that the initial pH value and $NaBF_4/Gd^{3+}$ molar ratios play important roles in the structures, sizes, and phases of the hollow products. The growth mechanism of the hollow spheres has been systematically investigated based on the Kirkendall effect. Under 980 nm IR laser excitation, UC luminescence of the as-prepared Yb^{3+}/Er^{3+}-codoped GdF_3 hollow spheres can be changed by a simple adjustment of the concentration of the Yb^{3+} ion. Enhanced red emission is obtained by introducing Li^+ ions in GdF_3:Yb^{3+}/Er^{3+}. Furthermore, a doxorubicin release experiment and a 3-[4,5-dimethylthiazol-2-yl]-2,5-diphenyltetrazolium bromide cytotoxicity assay reveal that the product has potential application in drug delivery and targeted cancer therapy.

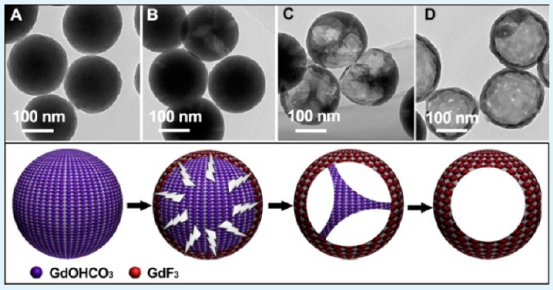

KEYWORDS: *GdF_3, spheres, hollow, luminescence, drug release, MTT*

INTRODUCTION

In recent years, hollow mesoporous-structured nano/microspheres with special functional properties (fluorescence, magnetism, etc.) have aroused many researchers' attention. Because of their distinct low density, high specific surface area, and particular channel structure, hollow mesoporous spheres have extensively been used as the most promising functional material in various biological fields such as drug carrying,[1−3] gene delivery,[4−7] cell labeling,[8,9] and photodynamic therapy.[10−13] Meanwhile, with the growing preparative method to create magnetic nanospheres, gadolinium-based compounds are widely applied in quantum dots,[14−17] protein purification,[18,19] magnetic targeted drug carrying,[20−22] and NMR imaging.[23−25] Magnetic targeting drug carrying is a significant result of nanotechnology combined with modern medicine, which has obvious advantages such as targeting property and biocompatibility. Moreover, rare-earth fluorides are of fundamental importance as up-conversion (UC) materials because of their low phonon energy, high luminous efficiency, and stable physical and chemical properties.[26−31] So, gadolinium fluorides with special functional structures and properties should be highly promising in diverse fields.

Up to now, most of researches on the hollow mesoporous spheres have focused on template-directed synthesis, which mainly contains two routes: hard and sacrificed templates. Hard templates usually use silica,[3,32−34] carbon spheres,[35] melamine formaldehyde,[36−38] and polystyrene beads[39,40] as the templates. After the templates are derived, hollow nanospheres were prepared. Using this method, hollow spherical inorganic materials could be acquired with especially beautiful morphology and pure phase. However, this method is disadvantaged because it is complicated to proceed with low yield and removal of the as-used template often brings about environmental concerns (used acid or base) and energy consumption (calcinations). Therefore, scientists have tended to find simple and easy methods to produce hollow spheres using the sacrificed template. Among the sacrificed-template synthesis routes, the Kirkendall effect has been proven to be an effective process to obtain the desired hollow nano/microspheres. Zhang et al. used one Y_2O_3 precursor to prepare $NaYF_4$ hollow spheres.[41] However, in his method, HF used as the pH-regulating solution and assistant fluorine source may bring problems such as burning of the skin, destruction of soft tissues, and induction of brittle-bone disease. Meanwhile, the precursor needed an annealing process, which was cumbersome and is not conducive to energy conservation. Most recently, Lin et al. demonstrated a strategy for the synthesis of monodisperse $GdPO_4$ hollow spheres using $Gd(OH)CO_3$ as the sacrificed

Received: July 23, 2013
Accepted: October 9, 2013
Published: October 9, 2013

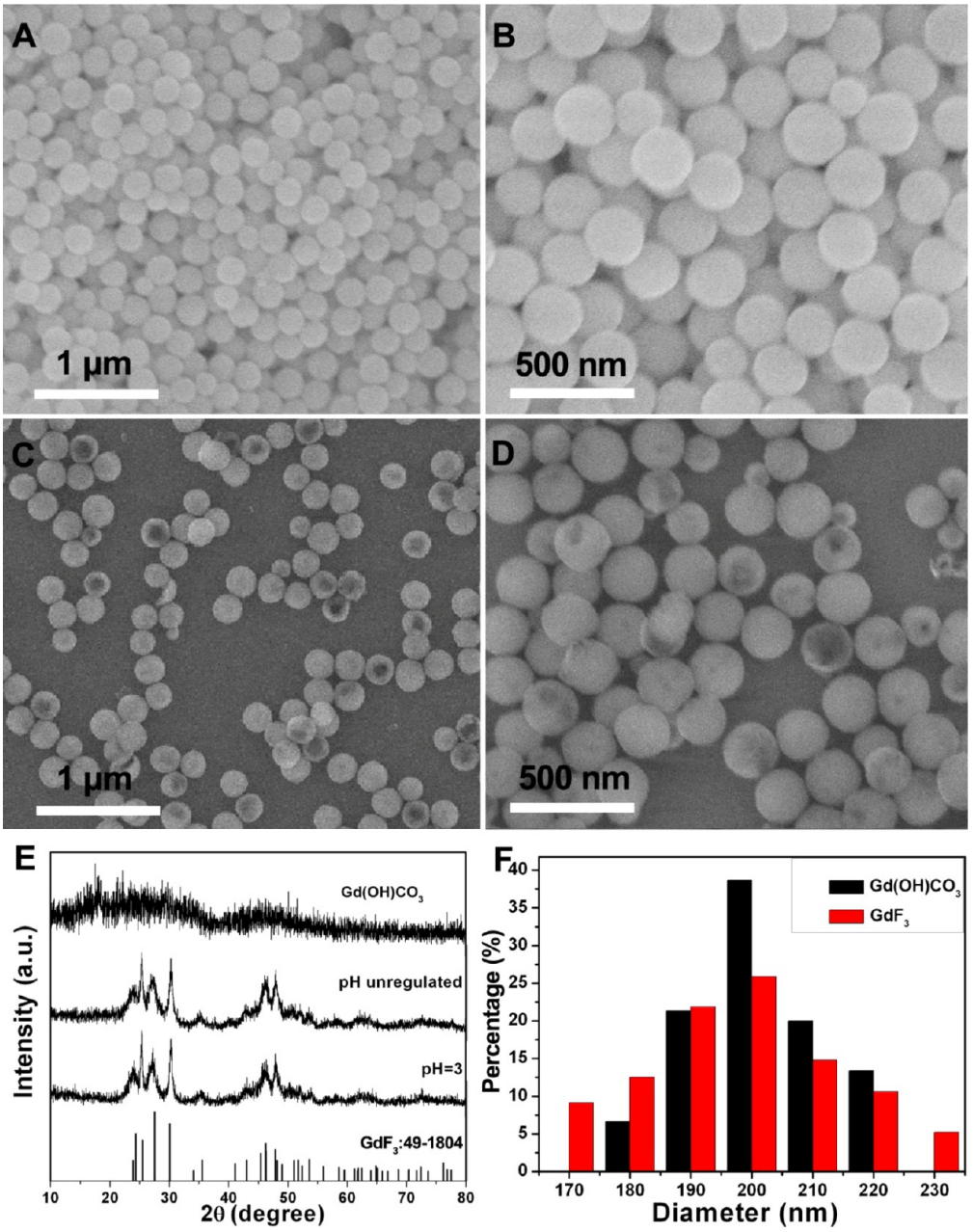

Figure 1. SEM images with low magnification (A) and high magnification (B) of the $Gd(OH)CO_3$ precursor and with low magnification (C) and high magnification (D) of GdF_3 after 5 h of reaction with the initial pH value unregulated. XRD patterns of $Gd(OH)CO_3$ and GdF_3 with different initial pH values (E). Diameter distribution diagram of $Gd(OH)CO_3$ and GdF_3 (F).

template.[42] In this report, $GdPO_4$ was used as down-conversion (DC) luminescence materials because of its high phonon energy of rare-earth material. However, the reaction temperature was high and the DC emission was less applicable than that of the UC materials in the biological application. Additionally, the size was nonadjustable with a microdiameter of 250 nm. In summary, a facile, user-friendly, and mild synthesis route to integrating diverse functions (porous structure, UC fluorescence, and magnetism) within one uniform material has rarely been reported.

In this study, $Gd(OH)CO_3$ prepared by coprecipitation was used as a sacrificed template to prepare the hollow mesoporous nanospheres based on the Kirkendall effect. $NaBF_4$ was used as the fluoride source; with a gradual release of H^+ and F^-, it made the hollow spheres evolve with ion exchange inside and outside the shell. Especially, we proposed a facile coprecipitation process with low temperature and short reaction time. The entire process was conducted in deionized water without the addition of any surfactant or catalyst. The effects of the initial pH value and $NaBF_4/Gd^{3+}$ molar ratios were altered to tune the sizes and phases of the product. Meanwhile, the UC fluorescent properties of GdF_3 codoped with Yb^{3+}/Er^{3+}, $Yb^{3+}/Er^{3+}/Li^+$, and Yb^{3+}/Ho^{3+} were investigated. Moreover, for a potential biomedical application, doxorubicin carried release measurement and 3-[4,5-dimethylthiazol-2-yl]-2,5-diphenyltetrazolium bromide cytotoxicity assays were also made.

EXPERIMENTAL SECTION

Reagents and Materials. All of the chemical reagents used in this experiment are of analytical grade without any further purification

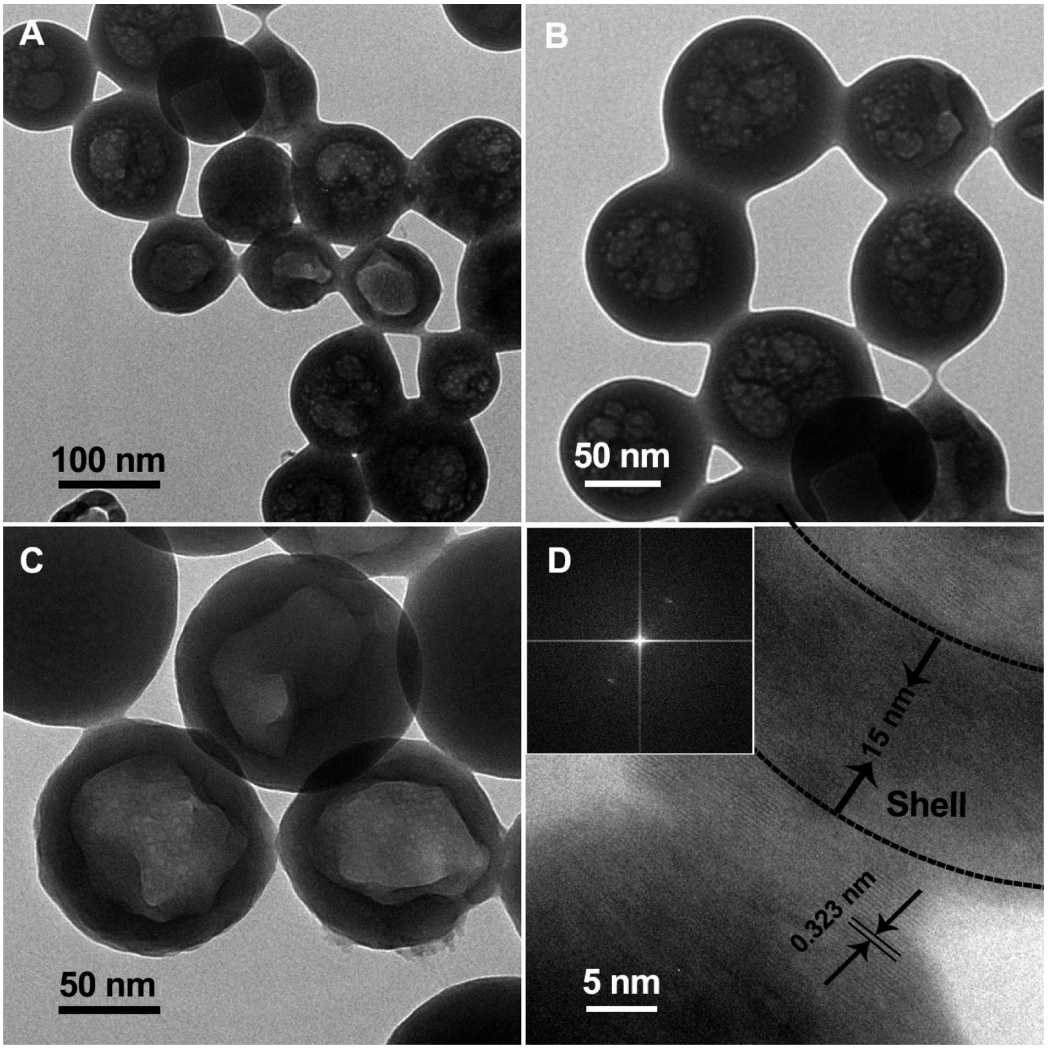

Figure 2. TEM images with different magnification (A–C) and HRTEM images of GdF_3 (D) with the initial pH value kept at 3 after 3 h of reaction.

including urea, concentrated nitric acid (HNO_3), lithium nitrate ($LiNO_3$), and sodium fluoroborate ($NaBF_4$) (from Beijing Chemical Corp.), Gd_2O_3 (99.99%), Yb_2O_3 (99.99%), Er_2O_3, and Ho_2O_3 (99.99%) (from Sinopharm Chemical Reagent Co., Ltd.), phosphate-buffered saline (PBS) and potassium hydrogen phthalate (PHP) (from Tianjin Kermel Chemical Reagent Co., Ltd.), and doxorubicin (DOX; from Nanjing Duodian Chemical Co. Ltd.). Rare-earth nitrate was obtained by dissolving the corresponding oxide in dilute HNO_3 followed by evaporation of water.

Synthesis. *Synthesis of Gd(OH)CO_3:Ln Nanosphere.* The monodisperse Gd(OH)CO_3 spheres were prepared via a precipitation process according to a published report[42] with some modification. In a typical process, 0.5 M $Ln(NO_3)_3$ were prepared by dissolving corresponding calculated Ln_2O_3 into HNO_3 with gradual heating. A total of 1 mL of 0.5 M $Gd(NO_3)_3$ and 1.5 g of urea were dissolved in 50 mL of deionized water in a beaker. After continuous stirring for 10 min, heating of the mixture was continued at 90 °C for 2 h through a water bath. The resulting mixture was centrifuged at 6000 rpm for 4 min. Then the supernatant solution was discarded, and the precipitate was washed with fresh deionized water. This process was repeated three times, and then the precursor Gd(OH)CO_3 was acquired. The preparation of lanthanide-doped Gd(OH)CO_3 spheres was similar to the above procedure except for the addition of a suitable amount of $Gd(NO_3)_3$, $Yb(NO_3)_3$, and $Er(NO_3)_3$ to replace pure $Gd(NO_3)_3$.

Synthesis of Gadolinium Fluoride Hollow Spheres. The as-prepared 0.5 mmol of the Gd(OH)CO_3:Ln sample was dispersed in 10 mL of deionized water, and then a certain amount of $NaBF_4$ was added in the solution with continuous stirring for 5 min at room temperature. Subsequently, the beaker was transferred to the water bath kettle kept at 50 °C. In order to discuss the effects of the initial pH value, the diluted HNO_3 solution (2 M) was used to regulate the pH value. After reaction for 3 h with an initial pH value of 3 or for 5 h with an initial pH value of 5, the resulting product were centrifuged three times and dried in a baking oven for 12 h .

DOX Release Experiment. A total of 0.03 g of the GdF_3:Yb^{3+}/Er^{3+}/Li^+ sample was added into 5 mL of PBS and then ultrasonically dispersed uniformly. After that, 0.0025 g of DOX was added into the solution with slow stirring at room temperature for 24 h. After DOX loading into the sample, the mixture was put in a centrifugal tube and centrifugally separated at 6000 rpm for 4 min, and the clear liquid was kept for UV–visible light analysis. Then 10 mL of fresh PBS was replenished in the centrifugal tube and set in the water bath kettle at 37 °C, and after stirring for 10 min, the supernatant liquid was kept. The experiment was repeated by changing the release time (e.g., 20, 30, 40, 50, and 60 min and 2, 4, 6, 8, 12, 24, and 48 h). PBS (pH 7) and PHP (pH 4) were prepared directly by a pH modifier.

In Vitro Cytotoxicity and Cell Viability of GdF_3:Yb^{3+}/Er^{3+}/Li^+. HeLa cells were plated out in 96-well plates at a density of 8000 cells per well and were grown overnight to allow cells to attach. GdF_3, DOX-GdF_3:Yb^{3+}/Er^{3+}/Li^+, and DOX were added to the media, and the cells were incubated in CO_2 (5%) at 37 °C for 24 h. The DOX concentrations were regulated to 0.3125, 0.625, 1.25, 2.5, and 5 μg/mL, respectively. Subsequently, 20 μL of a 3-[4,5-dimethylthiazol-2-yl]-2,5-diphenyltetrazolium bromide (MTT) solution was added to

each cell and incubated for another 4 h. The supernatant in each well was aspirated, and 150 μL of dimethyl sulfoxide was added before the plate was examined using a microplate reader (Therom Multiskan MK3) at a wavelength of 490 nm. The biocompatibility of the sample was also evaluated using a MTT cell assay on L929 fibroblast cells, which was the similar to the procedure for the cytotoxicity assay of GdF_3:Yb^{3+}/Er^{3+}/Li^+ spheres.

Characterization. Powder X-ray diffraction (XRD) patterns were measured on a Rigaku D/max TTR-III diffractometer at a scanning rate of 5°/min in the 2θ range from 20° to 80° with graphite-monochromatized Cu Kα radiation (λ = 0.15405 nm). Images were obtained digitally by scanning electron microscopy (SEM; JSM-6480A), transmission electron microscopy (TEM; FEI Tecnai G^2 S-Twin), and high-resolution TEM (HRTEM; FEI Tecnai G^2 S-Twin). UC emission spectra were acquired using a 980 nm LD Module (K98D08M-30W, China) as the excitation source and detected by R955 (Hamamatsu) from 400 to 750 nm. The specific surface area was determined by the Brunauer–Emmett–Teller (BET) method using data between 0.05 and 0.35, and the pore volume was obtained from the *t*-plot method. The DOX concentration was determined by a UV-601 spectrophotometer, and the absorbance scan value was recorded as 480 nm.

RESULTS AND DISCUSSION

Phase, Morphology and Texture Properties. It should be mentioned first that a low amount of doped ions did not change the phase, morphology, or crystallization of the resulting samples because of their very similar ionic radii. So, here we take the samples without doped ions as typical examples to demonstrate the products. Figure 1 shows the SEM images of the precursor and the resulting sample. We can see that there is obvious similarity in the size and shape. Parts A and B of Figure 1 show that the precursor is monodisperse with an average diameter of 200 nm, and the diameter distribution is narrow between 180 and 220 nm (Figure 1F). The SEM images prove that nucleation and growth of the $Gd(OH)CO_3$ precursor is homogeneous. Parts C and D of Figure 1 give images of the GdF_3 hollow spheres prepared at 50 °C for 5 h with the initial pH value unregulated. It can be seen that the resulting GdF_3 has size and morphology almost similar to those of the $Gd(OH)CO_3$ precursor, which suggests that the shape and size of the precursor is well preserved. Meanwhile, the diameter distribution of the resulting product becomes wider (170–230 nm) than that of the precursor. Figure 1E shows that $Gd(OH)CO_3$ does not have obvious diffraction peaks, indicating its noncrystalline nature. As for GdF_3 hollow spheres, the diffractions can be well indexed to the orthorhombic phase (JCPDS no. 49-1804). Furthermore, in order to make clear whether $Gd(OH)CO_3$ is still left in the product, we performed thermogravimetric (TGA), IR, and energy-dispersive spectrometry (EDS) analyses of the sample. From the TGA curve (Figure S1A in the Supporting Information, SI), we only can see a weight loss (4.6%) below 200 °C, which can be assigned to desorption of the physically adsorbed H_2O,[42,43] and no weight loss associated with decomposition of $Gd(OH)CO_3$ (over 500 °C) can be found.[44] In the IR spectrum of GdF_3 (Figure S1B in the SI), the absorption peaks at 1523, 1401, 843, 753, and 688 cm^{-1} associated with the vibrations of CO_3^{2-} almost disappear compared with $Gd(OH)CO_3$. As shown in EDS, the peaks (signals) assigned to the C and O elements can hardly be detected, the total atomic ratio of the two elements is less 0.3%, which can nearly be neglected. All of the results indicate the pure phase of the sample and complete conversion from the $Gd(OH)CO_3$ precursor to GdF_3 hollow spheres.

When the initial pH value of the second-step reaction is decreased to 3, the resulting product will become the smaller one with an average diameter of 100 nm (Figure 2A) due to dissolution of the precursor. The effects of the pH value will be discussed in detail in the next part. From the TEM images with different magnifications, we can clearly see that there is a strong contrast between the darker shell and brighter inside, indicating the hollow structure of the resulting product. As shown in Figure 2B, there are obvious mesopores in the center of the hollow spheres. Figure 2C further reveals that the thickness of shell is about 15–25 nm. Figure 2D represents the apparent lattice fringes between the two hollow shells. The interplanar distance between the adjacent fringes is calculated to be 0.323 nm, which can exactly be in conformity with the (111) plane spacing of GdF_3. The corresponding Fourier transform pattern (inset in Figure 2D) shows the diffraction spots of the (111) planes of GdF_3 and reveals the single-crystalline nature of the sample.

In order to ascertain formation of the mesoporous structure, a N_2 adsorption/desorption experiment of GdF_3 prepared with the initial pH value unregulated was carried out. It can be seen from Figure 3A that the sample exhibits typical IV-type

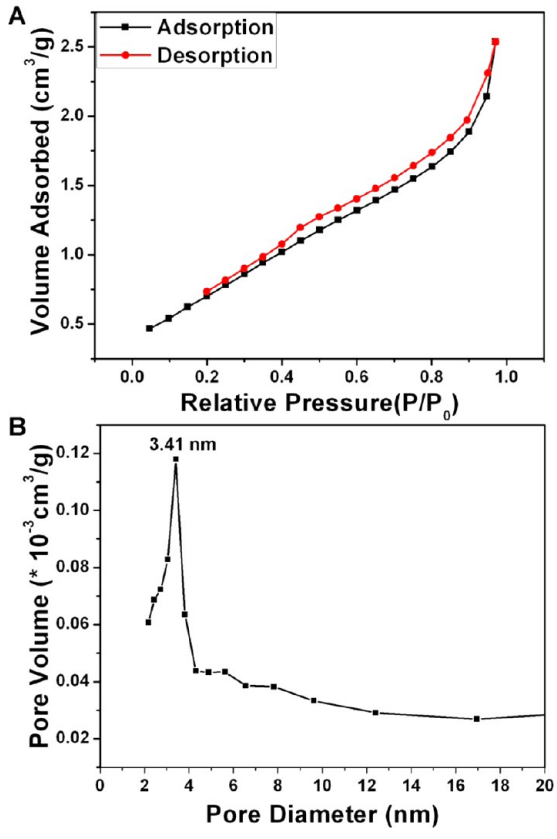

Figure 3. N_2 adsorption/desorption isotherm of a mesoporous GdF_3 sample (A) and the corresponding pore-size distribution curve (B).

isotherms with H1 hysteresis loops, which show the characteristics of typical mesoporous materials.[45] The BET surface area and total pore volume are calculated to be 45.6 m^2/g and 0.0647 cm^3/g. As shown in Figure 3B, we can see that the pore diameter is about 3.4 nm.

Growth Mechanism of Hollow Spheres. To explain the evolution of the hollow spheres, step-dependent experiments were carried out. From Figure 4, we can see that the solid

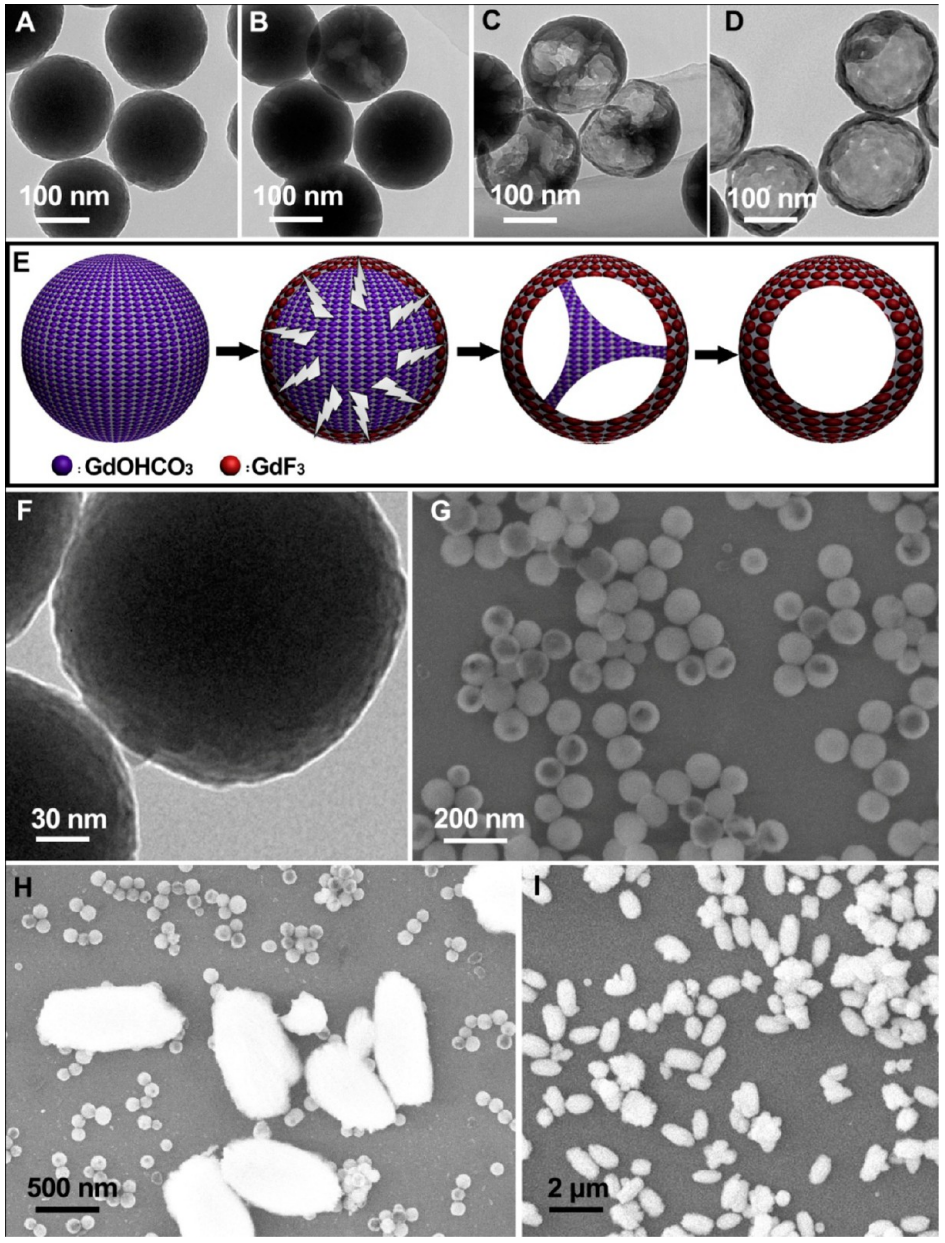

Figure 4. TEM images of GdF_3 prepared for 0 h (A), 30 min (B), 3 h (C), and 5 h (D) with a $NaBF_4/Gd^{3+}$ molar ratio of 8 and the initial pH value unregulated. Schematic representation of the hollow spheres formation process based on the Kirkendall effect (E). TEM images of $Gd(OH)CO_3$ with high magnification (F). SEM images of GdF_3 prepared for 3 h (G), 6 h (H), and 15 h (I) with a $NaBF_4/Gd^{3+}$ molar ratio of 8 and the initial pH value kept at 3.

spheres changed to hollow ones with an increase of the reaction time. Parts A–D of Figure 4 show the TEM images of GdF_3 prepared for the reaction time from 0 to 5 h with a $NaBF_4/Gd^{3+}$ molar ratio of 8 and the initial pH value unregulated. From Figure 4A, we can see that the precursor consists of solid spheres with an average diameter of 200 nm. Close observation of the TEM images with high magnification (Figure 4F) reveals that the large spheres are made of tiny nanospheres, which can be seen from the composition of the circular arc curves around the large sphere. The interspaces between the constituent tiny particles provide space for the H^+ ions deriving from hydrolysis of $NaBF_4$ to pass through. Meanwhile, $Gd(OH)CO_3$ dissolves to Gd^{3+}, OH^-, and CO_3^{2-}. Then Gd^{3+} ions precipitate to GdF_3 with F^- ions. OH^- and CO_3^{2-} dissolve into the solution, and the decreased $Gd(OH)CO_3$ spheres may proceed the continuous reaction. As demonstrated in Figure 3B, after for 30 min of reaction, some irregular pores appear on the surface of the spheres. As the reaction proceeds, the H^+ ions dissolve and the F^- ions precipitate the residual $Gd(OH)CO_3$, and the GdF_3 shell is formed. As the reaction time is increased to 3 h (Figure 4C), there are only a few bridges connected between the shell and center of survived $Gd(OH)CO_3$, which appear like the three-pointed star. When the reaction time is up to 5 h, the hollow spheres are acquired without any precursor inside (Figure 4D). In this step-by-step process, the F^- ion plays an important role in formation of the final product as the exchange ion. The concentration of the F^- ion needs to be controlled; otherwise, the solid spheres or other phases will be formed, which will be discussed below. The whole process can be well

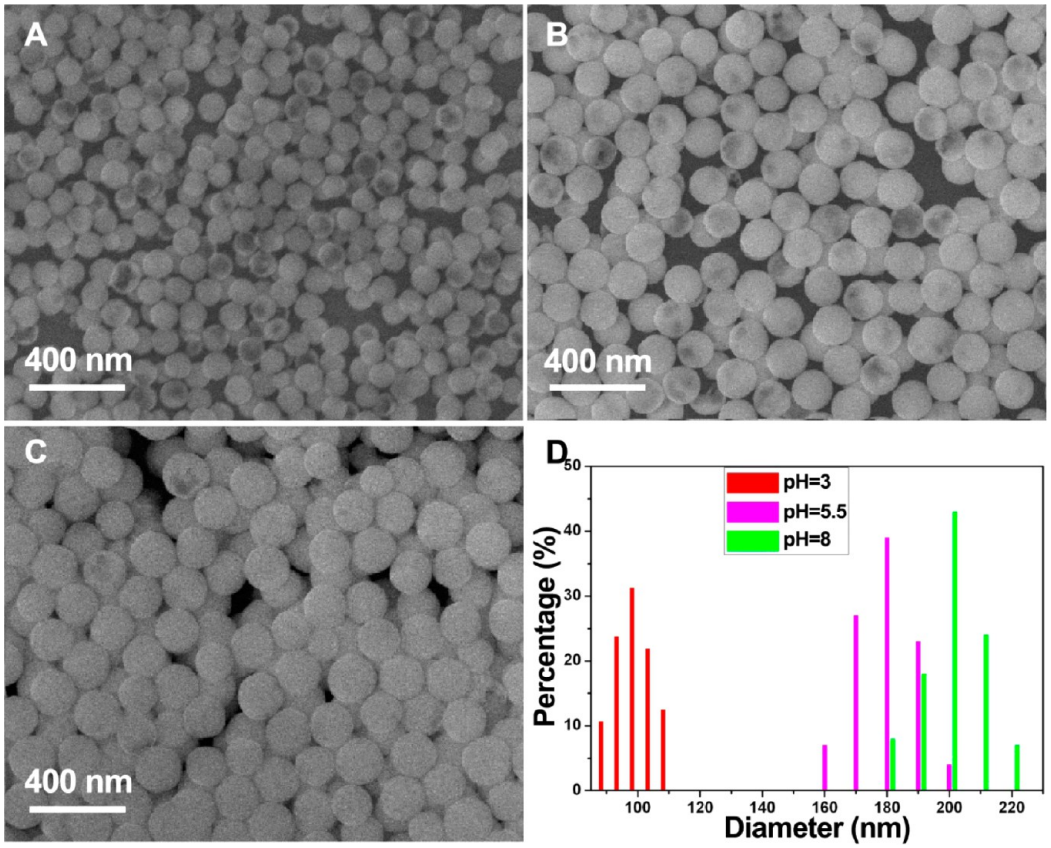

Figure 5. SEM images of GdF_3 prepared for 3 h with a $NaBF_4/Gd^{3+}$ molar ratio of 8 and pH values of 3 (A), 5.5 (B), and 8 (C). Diameter distribution diagram of GdF_3 with different pH values (D).

consistent with the Kirkendall effect, which is schematically presented in Figure 4E.

Parts G–I of Figure 4 show the SEM images of GdF_3 prepared for 3, 6, and 15 h with a $NaBF_4/Gd^{3+}$ molar ratio of 8 and the initial pH value kept at 3. It can be seen that uniform hollow spheres are obtained for 3 h. With the coprecipitation proceeding, H^+ and BO_3^{3-} ions in the solution play the role of surfactants in crystal nucleation. Because the growth rate in the [001] direction is higher with a larger capping scale in the (001) plane, the length of the resultant product increases,[46] and a rodlike phase appears (Figure 4H) accompanied with hollow spheres. When the reaction time is up to 15 h, the product is composed of rodlike and irregular blocks without any hollow sphere (Figure 4I). That means that the reaction time of 3 h is the optimum value to acquire good morphology and pure phase when the initial pH value is 3.

Influential Factors on the Phase and Size. In this section, the morphology and size of the samples prepared with different initial pH values and varying $NaBF_4/Gd^{3+}$ molar ratios will be investigated in detail.

Effect of the pH Value. Figure 5 shows the effect of the initial pH value on the size and quantity of the hollow spheres. From Figure 5A, when the initial pH value is 3, the resulting product is composed of a great number of hollow nanospheres with an average diameter of 100 nm, which is also confirmed by the TEM images (Figure 2). In Figure 5B, the resulting product prepared at a pH value of 5.5 contains less hollow spheres with an increasing diameter of about 180 nm. When the pH value is increased to 8, there are few hollow spheres but solid ones with a diameter of 200 nm (Figure 5C). These changes can be explained by the role of the pH values in the GdF_3 formation process. In fact, the hollow spheres are acquired with corrosion of the precursor. There are two procedures in the reaction. First, $Gd(OH)CO_3$ is hydrolyzed to the Gd^{3+}, OH^-, and CO_3^{2-} ions. Meanwhile, BF_4^- is hydrolyzed to the F^- and H^+ ions. Second, the Gd^{3+} and F^- ions then precipitate to GdF_3. The rate of the first procedure determines the diameter of the products, while the structure (hollow or solid) is decided by the relative rate of the second procedure. The two procedures can be shown by the following equations:

$$Gd(OH)CO_3 \rightarrow Gd^{3+} + OH^- + CO_3^{2-} \quad (1\text{-}1)$$

$$BF_4^- + 3H_2O \rightarrow BO_3^{3-} + 6H^+ + 4F^- \quad (1\text{-}2)$$

$$Gd^{3+} + 3F^- \rightarrow GdF_3 \quad (2\text{-}1)$$

The significant effect of the initial pH value on the size of the hollow spheres is explained as follows. When the initial pH value is 3, the reaction system contains many H^+ ions itself at the beginning. According to the chemical reaction balance law, the hydrolysis process of BF_4^- will be restrained in the solution with a high H^+ ion concentration. Then eq (1-2) will have difficulty proceeding, so the reaction environment has a low concentration of F^- ions. However, the high concentration of H^+ ions is beneficial to dissolution of the precursor $Gd(OH)CO_3$, so the large $Gd(OH)CO_3$ spheres (Figure 1A,B; 200 nm in diameter) separate to smaller ones (100 nm in diameter). After the separation process, the reaction will proceed according to the equations. When the initial pH value is adjusted to 5.5, the reaction system contains fewer H^+ ions, so

eq (1-2) will carry on more quickly, which makes F^- release rapidly. With a decrease of the H^+ ion, large $Gd(OH)CO_3$ spheres stop dividing into smaller ones, so the diameter of the products remains similar to that of the precursor with an average of 180 nm. When the initial pH value is up to 8, the concentration of H^+ ions is much lower, and the dissolution of $Gd(OH)CO_3$ terminates, so the diameter is about 200 nm, which almost remains the same as the precursor.

The amount of hollow spheres prepared with different initial pH values will also be discussed. Comparing the three images in Figure 5, we can see that the amount of hollow spheres decreases with an increase of the pH value. This is because the formation of hollow spheres through a sacrifice-template method based on the Kirkendall effect is attributed to the different diffusion rates between two components in a diffusion couple. In this reaction process, the diffusion couples are the Gd^{3+} ion inside and the F^- ion outside deriving from hydrolysis of BF_4^- ions, which will be precipitated as eq (2-1). In the case of low-pH-value conditions, more H^+ ions will react with the core $Gd(OH)CO_3$, producing a large amount of Gd^{3+}. Meanwhile, a large amount of H^+ ions will inhibit hydrolysis of BF_4^-, resulting in the low concentration of F^- ions. The two functions lead to different diffusion rates between F^- ions outside and Gd^{3+} ions inside when the pH value is low. It is known that if the diffusion rate of Gd^{3+} ions from inside to outside is faster than that of F^- from outside to inside, Kirkendall voids will be generated, leading to the formation of hollow spheres,[47,48] while under the condition of a high pH value, the low H^+ concentration promotes hydrolysis of BF_4^- to produce F^- and H^+ ions. The formation of GdF_3 from as-produced F^- and Gd^{3+} deriving from the reaction between as-produced H^+ and $Gd(OH)CO_3$ takes place on the outside of the core spheres, giving rise to the formation of GdF_3 solid spheres. Scheme 1 gives a schematic illustration for the structure and phase evolution of GdF_3 prepared with different initial pH values.

Scheme 1. Illustration for the Morphology Evolution of GdF_3 with Different pH Values

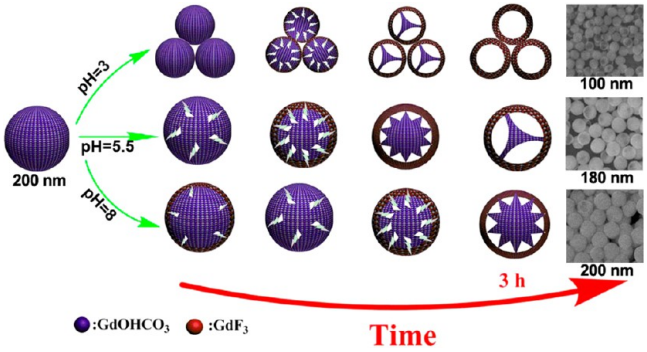

Effect of the $NaBF_4/Gd^{3+}$ Molar Ratio. In Figure 6A for the sample prepared with a $NaBF_4/Gd^{3+}$ molar ratio of 2, the peaks can be associated with noncrystalline $Gd(OH)CO_3$, indicating that probably no gadolinium fluoride is formed. For the sample prepared with ratios of 8 and 12, the diffraction peaks indicate that the products are orthorhombic GdF_3 (JCPDS no. 49-1804). When the $NaBF_4/Gd^{3+}$ molar ratio is increased to 16, the diffraction peaks can be assigned to $Na_5Gd_9F_{32}$ (JCPDS no. 27-0698). Also, cubic-phased $NaGdF_4$ (JCPDS no. 27-0697) is obtained as a ratio is up to 20.

From parts B to F of Figure 6, it is obvious that the sizes of the hollow spheres are different with altered molar ratio. When the ratio is 2, the concentration of H^+ and F^- ions deriving from hydrolysis of BF_4^- is low, which means less F^- ions participate in the formation of gadolinium fluoride. Meanwhile, the low concentration of H^+ ions cannot create enough space inside the sphere. So, the product is mainly made up of solid $GdOHCO_3$ spheres without reaction with $NaBF_4$ (Figure 6B). When the ratio is increased to 8, the diameter of the product is about 200 nm with an increased amount of hollow spheres (Figure 6C). As H^+ and F^- ions are hydrolyzed more and more by BF_4^-, the increased H^+ ions are favorable for the separation and solution of $Gd(OH)CO_3$, resulting in smaller hollow spheres. The smaller hollow spheres (about 170 nm) are obtained when the ratio is 12 (Figure 6D). If the ratio is further increased to 16, we can see the size of the spheres remain at 170 nm (Figure 6D,E) except that the crystal phase changes to $Na_5Gd_9F_{32}$. When the molar ratio is increased to 20, uniform $NaGdF_4$ hollow spheres with an average diameter of 150 nm are obtained (Figure 6F). Scheme S1 in the SI gives a schematic illustration for the structure and phase evolution of gadolinium fluorides prepared with different $NaBF_4/Gd^{3+}$ molar ratios.

UC Luminescent and Magnetic Properties. It is well-known that the efficiency of energy conversion is mainly decided by the matching extent of the excitation photon energy and rare-earth-ion energy level. Meanwhile, low phonon energy of the matrix material also plays a significant role. Rare-earth fluorides[49−56] have been extensively applied as the UC photoluminescence materials because of their low phonon energy, high luminous efficiency, and good stability. In this report, the luminescent properties of Yb^{3+}/Er^{3+}-, $Yb^{3+}/Er^{3+}/Li^+$-, and Yb^{3+}/Ho^{3+}-doped GdF_3 hollow spheres were investigated. All of the samples were prepared with the same reaction time of 5 h, and the molar ratio remained at 8 with the initial pH value unregulated.

UC Luminescent Properties of GdF_3:Yb^{3+}/Er^{3+}. Yb^{3+}/Er^{3+}-codoped rare earths are well accepted as the UC luminescence materials that are studied by many scientists.[57−61] Figure 7A shows the UC emission spectra of GdF_3:x%Yb^{3+}/1%Er^{3+} with altered Yb^{3+} concentration from 5% to 40%. Through integration of the green (500−600 nm) and red (600−700 nm) regions, Figure 7B clearly shows that the integral of red spectra becomes higher while the integral of green spectra becomes lower. With an increase of the Yb^{3+} concentration, the red-to-green emission ratio changes from the initial value of 0.80 to 2.05. Accordingly, the emission color changes from green (5−15%) to yellow-green (20−30%) and then to yellow (40%). In Figure 7C for the representative GdF_3:15%Yb^{3+},1% Er^{3+}, the spectrum contains three main emission peaks at around 521, 540, and 655 nm, corresponding to $^2H_{11/2} \rightarrow {}^4I_{15/2}$, $^4S_{3/2} \rightarrow {}^4I_{15/2}$, and $^4F_{9/2} \rightarrow {}^4I_{15/2}$. Additionally, a weak emission peak at 490 nm assigned to $^2H_{9/2} \rightarrow {}^4I_{15/2}$ can also be detected. In general, the emission is not observed because of the low efficiency of the three/four-photon UC process and strong scattering of the host lattices. This appearance further proves that the resulting GdF_3 samples are good hosts because of the low phonon energy of the host lattice. However, the intensity of the blue region changes little with variation of the Yb^{3+} ion concentration because of the quenching caused by surface defects. As the concentration of Yb^{3+} ions is changed, the transformation of the green and red regions is different because the activator Er^{3+} ion on UC luminescence depends on energy transfer of the sensitizer Yb^{3+} ion. The excitation power-

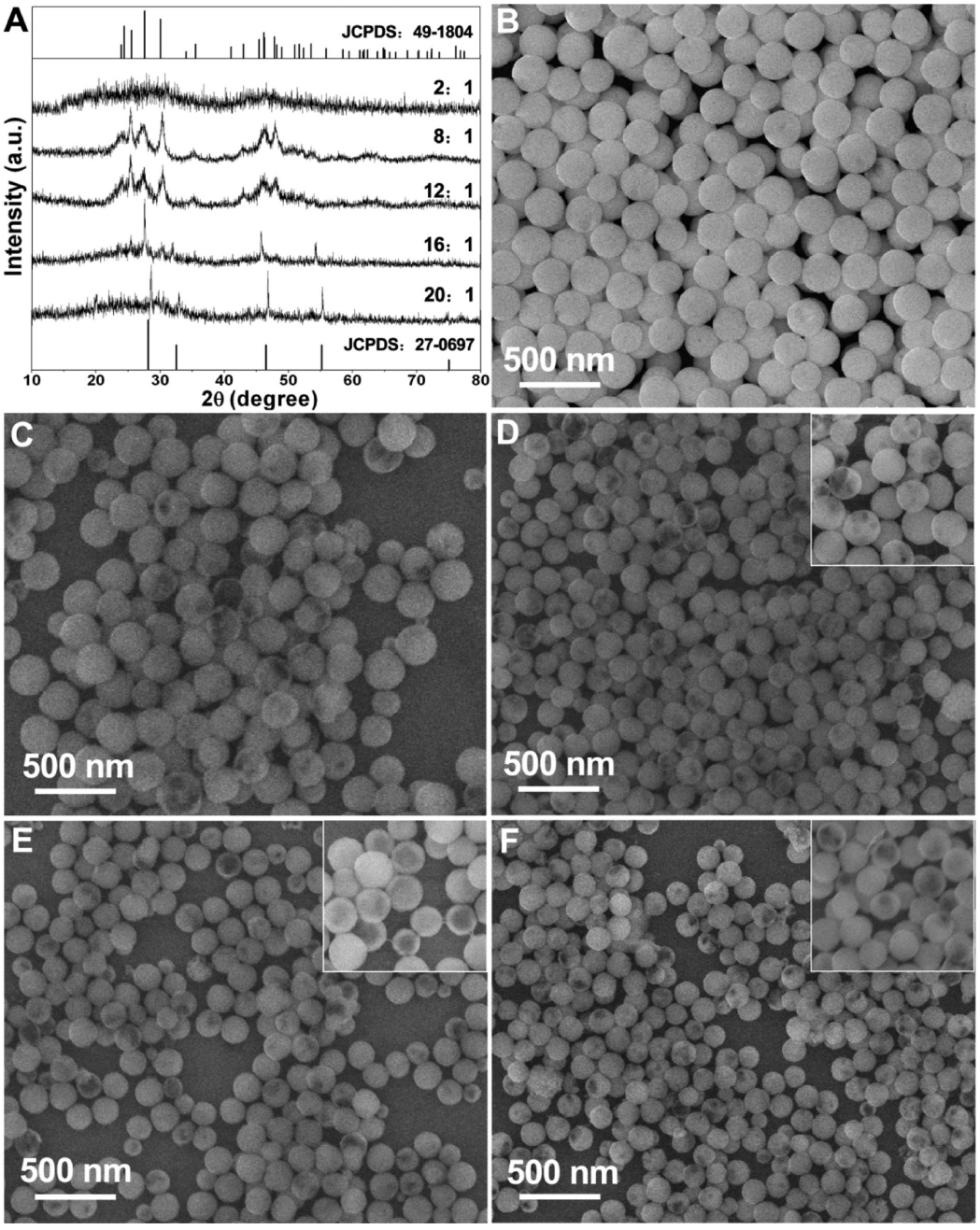

Figure 6. XRD patterns of the products prepared with different molar ratios (A). SEM images of the products with $NaBF_4/Gd^{3+}$ molar ratios of 2:1 (B), 8:1 (C), 12:1 (D), 16:1 (E), and 20:1 (F). All of the products were prepared for 5 h with the initial pH value unregulated.

dependent UC emissions of the green and red intensity of GdF_3:15%Yb^{3+}/1%Er^{3+} were also detected and calculated for the purpose of inspecting the related UC mechanism, as shown in Figure 7D. It is well accepted that the output luminescent intensity (I) is a function of the IR excitation power (P), which is signified by the formula $I \propto P^n$, where n is the absorbed photon numbers by the ground-state level during the energy-transfer process.[62] After taking the logarithm of the green and red emissions and the IR excitation power, the respective ratios are 1.88 and 1.74, which indicates that the two emission processes are both two-photon. On the basis of these explanations, the possible related energy-transfer process of GdF_3:Yb^{3+}/Er^{3+} is demonstrated in Figure 7E. The CIE chromaticity diagram (Figure S2 in the SI) reveals that the luminescence is changed from green to yellow. In summary, the UC luminescence of the as-prepared GdF_3:Yb^{3+}/Er^3 can be tuned by a simple adjustment of the concentration of Yb^{3+} ions under 980 nm IR excitation.

UC Luminescent Properties of GdF_3:Yb^{3+}/Er^{3+}/Li^+. Wang et al. have demonstrated a strategy to tune the UC luminescent emission by doping different concentrations of Li^+ ions into $NaYF_4$:Yb^{3+}/Er^{3+}.[63] The changed UC emissions were probably due to the tailoring effect of the Li^+ ions. We also tried to introduce Li^+ ions into the GdF_3 host to tune the UC emission. Figure S3A in the SI shows the UC emission spectra of GdF_3:15%Yb^{3+}/1%Er^{3+}/y%Li^+ (y = 0, 3, 6, 9, and 12). As shown, GdF_3:Yb^{3+}/Er^3 without doping Li^+ ion shows three visible peaks dominated by the green emission. With increased Li^+ in GdF_3:15%Yb^{3+}/1%Er^{3+}, the emission changes from green to orange. As demonstrated in Figure S3Ba in the SI, the

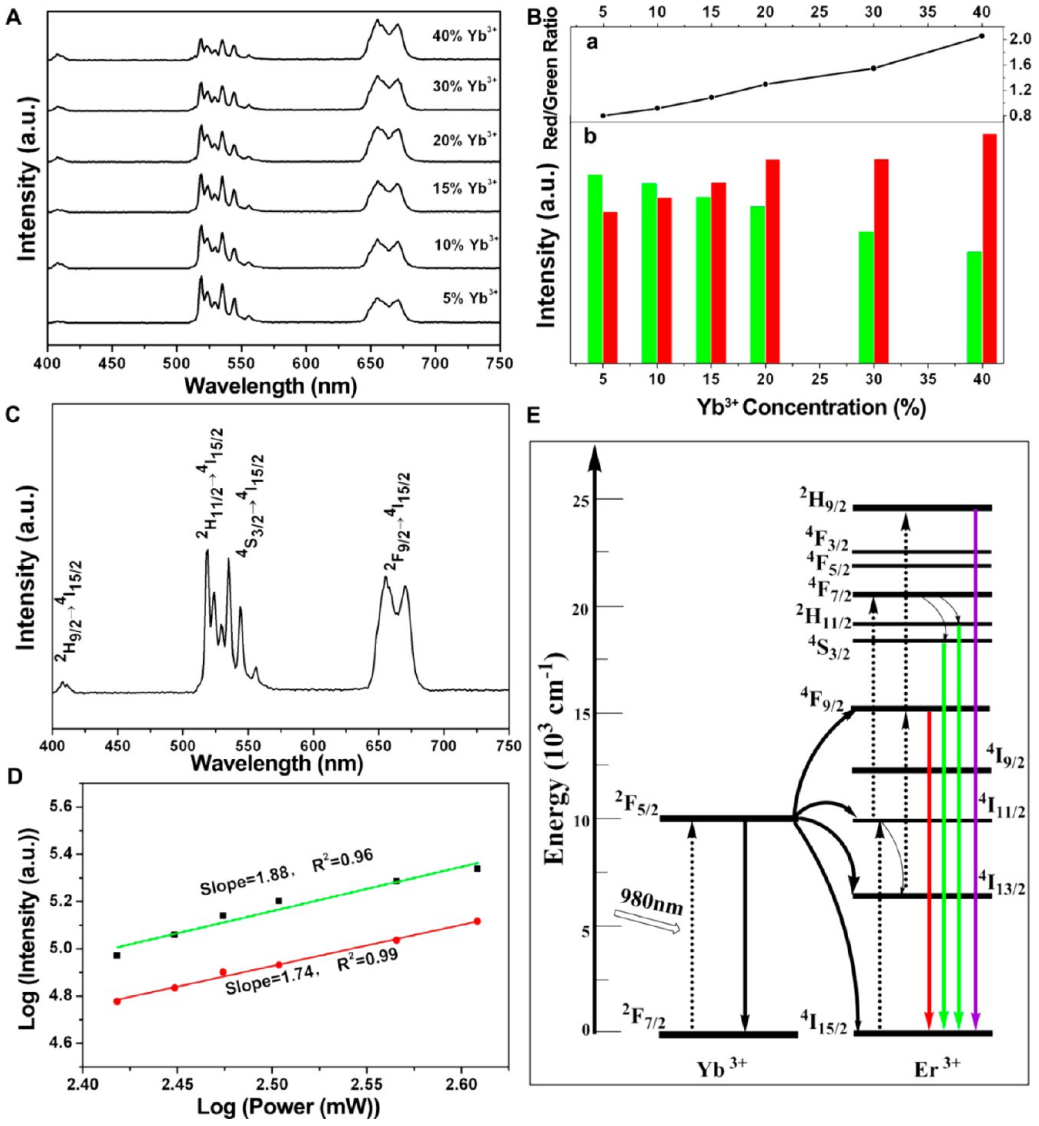

Figure 7. UC luminescence spectra of GdF_3:x%Yb^{3+},1%Er^{3+} (x = 5, 10, 15, 20, 30, and 40) under 980 nm excitation (A). Red/green ratio (a) and integral intensity of the green and red emissions (b) as a function of the doped Yb^{3+} concentration (B). Emission spectrum of GdF_3:15%Yb^{3+},1%Er^{3+} (C). Red and green emission intensity relationship with dependence of the laser pump power (D). Energy-transfer mechanism of GdF_3:Yb^{3+},Er^{3+} using an energy level diagram (E).

intensity of the red/green ratio is 7.05 when the Li^{3+} concentration is 12%, which is about 7 times higher than that of GdF_3:Yb^{3+}/Er^{3+} without Li^+ (1.07). Figure S3Bb in the SI shows that the green emission intensity gradually decreases with the doped concentration of Li^+. When the concentration of Li^+ increases to 12%, the green region almost disappears. Meanwhile, the emission of the red region initially increases with the Li^+ concentration from 0 to 6% and then decreases slightly with further enhanced concentration. Interestingly, the purple light (409 nm) disappears for the Li^+-doped sample, which means that the doped Li^+ makes a three-photon process ($^4F_{9/2} \rightarrow {}^2H_{9/2}$) disappear, which causes an increase of the phonon number of the $^4F_{9/2}$ level in order to enhance the red emission. Furthermore, the energy back-transfer process $^4S_{3/2}$(Er) + $^2F_{7/2}$(Yb) → $^4I_{13/2}$(Er) + $^2F_{5/2}$(Yb) could also populate the $^4I_{13/2}$(Er) state, and the $^4F_{9/2}$(Er) state is populated by excitation via energy transfer of the saturated $^4I_{13/2}$(Er) state, which enhances red light and decreases green light.[64] The two functions are beneficial to the enhancement of the red region. And the luminescence is changed from green to orange which is shown in Figure S3C in the SI. In brief conclusion, low concentration of doping Li^+ ion into GdF_3:Yb^{3+},Er^{3+} makes the chief emission region vary from green (521 and 540 nm) to red (650 nm).

UC Luminescent Properties of GdF_3:Yb^{3+}/Ho^{3+}. It is well-known that a Yb^{3+}/Ho^{3+}-doped rare-earth fluoride such as $NaREF_4$[65−67] and REF_3[68,69] emits strong green light under IR excitation. In this study, UC luminescence of GdF_3:x%Yb^{3+}/1% Ho^{3+} (x = 5, 10, 15, 20, and 30) with hollow structures was also studied. Figure 8A shows the UC emission spectra of GdF_3:x% Yb^{3+}/1%Ho^{3+} with different Yb^{3+} concentrations. A strong emission band located from 541 to 548 nm and a broad weaker emission band at 646−665 nm are observed, which can be associated with $^5F_4/{}^5S_2 \rightarrow {}^5I_8$ and $^5F_5 \rightarrow {}^5I_8$ transitions of Ho^{3+} ions, respectively. Similar to GdF_3:Yb^{3+}/Er^{3+}, in the purple region of GdF_3:Yb^{3+}/Ho^{3+}, a weak emission peak at 461 nm corresponds to the $^5F_1 \rightarrow {}^5I_8$ transition and the intensity changed little with altered Yb^{3+} concentration. Different from

dx.doi.org/10.1021/am4041652 | ACS Appl. Mater. Interfaces 2013, 5, 10806−10818

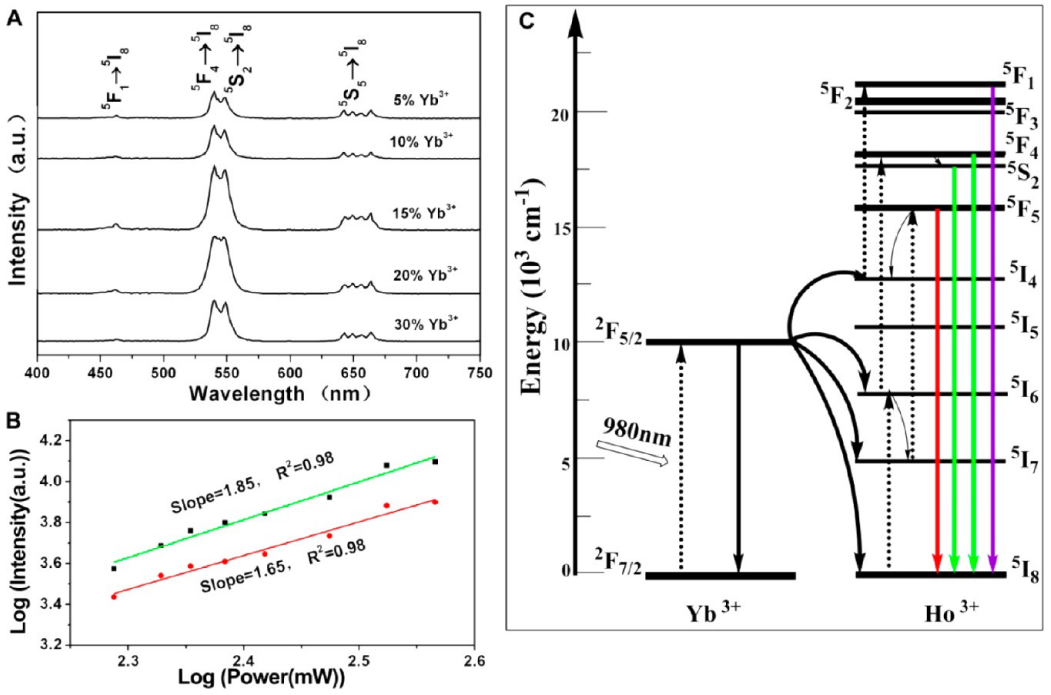

Figure 8. UC luminescence spectra of GdF_3:*x*%Yb^{3+},1%Ho^{3+} (*x* = 5, 10, 15, 20, and 30) under 980 nm excitation (A). Red and green emission intensity relationship with dependence of the laser pump power of GdF_3:15%Yb^{3+},1%Ho^{3+} (B). Energy-transfer mechanism of GdF_3:Yb^{3+},Ho^{3+} using the energy level diagram (C).

GdF_3:Yb^{3+}/Er^{3+}, these two main regions (green and red) display little difference with the altered Yb^{3+} concentration. With an increase of the Yb^{3+} concentration lower than 15%, the intensity of each emission region enhances. With higher concentration (15−30%), the emission intensity remains almost stable with little decreasing tendency, which may be due to the quenching effect. The power-dependent green and red emissions in GdF_3:15%Yb^{3+}/1%Ho^{3+} under 980 nm excitation are shown in Figure 8B. The slopes of the green and red emissions between the integral intensity and dependent power are 1.85 and 1.65, respectively. The result shows that red- and green-emitting processes are both two-photon energy-transfer ones. On the basis of these results, the possible related energy-transfer process of GdF_3:Yb^{3+}/Ho^{3+} is displayed in Figure 8C.

Magnetic Properties. The magnetization as a function of the applied magnetic field (from −10 to +10 kOe) for GdF_3 hollow spheres is given in Figure S4 in the SI. It is apparent that the sample shows typical paramagnetic properties. The magnetic behavior should be due to the unpaired inner 4f electrons, which are closely bound to the nucleus and effectively shielded by the outer $5s^25p^6$ electron.[70] In this study, the magnetic moments related with the Gd^{3+} ions are localized and noninteracting, which give rise to paramagnetism.[71]

Cell Vialiability, Drug Release, and MTT Cytotoxicity. *Cell Viability of GdF_3:Yb^{3+}/Er^{3+}/Li^+.* For potential biological application, it is essential to evaluate the biocompatibility of the proposed material. Standard MTT cell assay was carried on L929 cell lines in order to detect the viability of GdF_3:Yb^{3+}/Er^{3+}/Li^+ hollow spheres.[72] Figure 9 demonstrates the cell viability with different concentrations of GdF_3:Yb^{3+}/Er^{3+}/Li^+ varying from 7.8125 to 500 μg/mL incubated for 24 h. It is obviously shown that the biocompatibility of the as-prepared material in all dosages is up to 99−105%. Even at a high-dose concentration of 500 μg/mL, there are still 104.89% cells

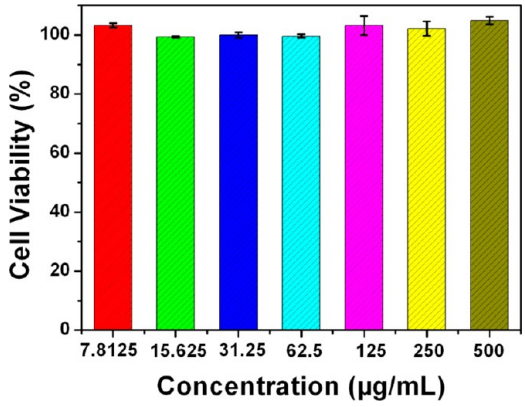

Figure 9. L929 fibroblast cell viability incubated for 24 h with GdF_3:Yb^{3+}/Er^{3+}/Li^+ hollow spheres of different concentrations.

observed. It should be pointed out that when the sample has good biocompatibility, a cell viability of higher than 100% is a normal state because the cells multiply at an abnormally rapid rate, which has been reported extensively.[73,74] The MTT assay data demonstrated that these hollow spheres are nontoxic to live cells and can be potentially applied in biotechnology as drug carriers.

Drug Loading and Release Properties. DOX was selected as a model drug to evaluate the loading and controlled release behaviors of hollow spheres. After being continuously stirred for 24 h, DOX has been almost completely convergent to GdF_3:Yb^{3+}/Er^{3+}/Li^+ with a loading efficiency of 88.3%. Additionally, we detected pH-dependent drug-release behavior. The pH value of normal cells in the human body is nearly neutral, and the pH value of cancer cells is decreased, which is caused by the excess metabolic product due to the fast proliferation of cancer cell. Here, pH values of 4 and 7 are selected to investigate the release efficiency. As shown in Figure

10, only 30.9% of DOX was released from the carrier when the pH value is 7. By contrast, the carrier shows a fast drug-release

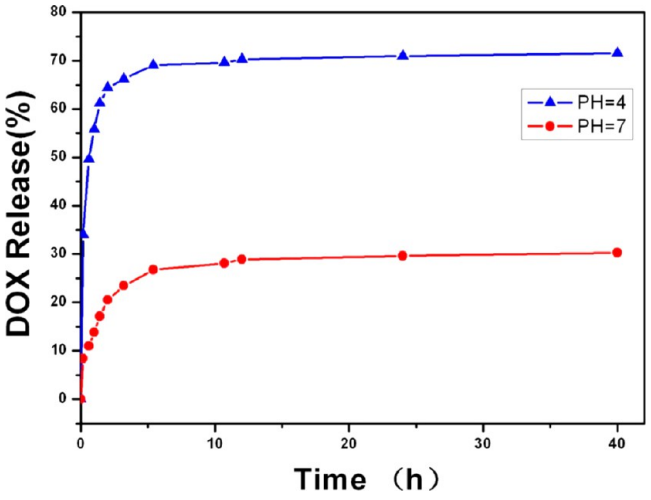

Figure 10. Cumulative DOX release from DOX−GdF_3:Yb/Tm/Li with release time at pH values of 4 and 7.

rate when the pH value is 4. During the beginning of 1 h, 55.8% of DOX was released. Also, 71.6% of DOX has released after 40 h. The initially rapid release of DOX molecules is essential to the treatment of cancer because the fast release of an anticancer drug can efficiently inhibit the growth of cancer cells. After that, the slow release of the rest of the drug molecules can be continued for curbing the few surviving cells from the first stage. Because of the high efficiency of the loading drug and fast release process, the as-prepared hollow mesopores GdF_3:Yb^{3+}/Er^{3+}/Li^+ are potentially applied in the drug-delivery system.

MTT Cytotoxicity Assay. Cellular cytotoxicity is an important factor in evaluating the potential application of the drug-delivery system. To investigate the pharmacological activity of the DOX-loaded spheres, the cytotoxic effect of DOX-loaded GdF_3:Yb^{3+}/Er^{3+}/Li^+ on HeLa cells is valuated in vitro via MTT assay.[73,74] As shown in Figure 11, when GdF_3:Yb^{3+}/Er^{3+}/Li^+ is used as the drug carrier, more than 100% Hela cells are viable under a varying concentration range,

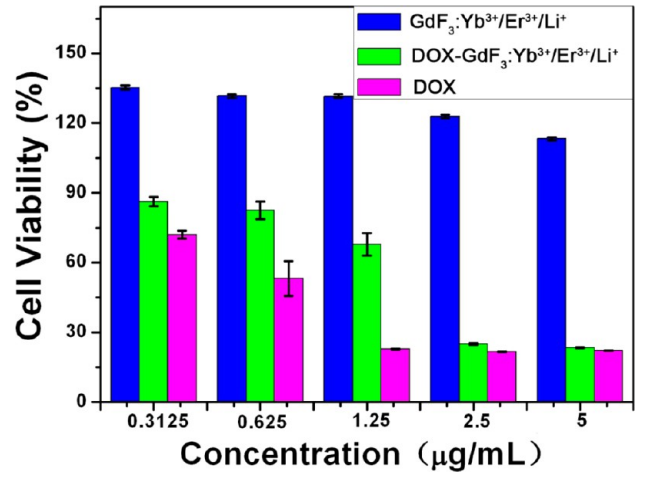

Figure 11. In vitro HeLa cell viabilities incubated for 24 h with free DOX, DOX−GdF_3:Yb^{3+}/Er^{3+}/Li^+, and pure GdF_3:Yb^{3+}/Er^{3+}/Li^+ of different concentrations.

which indicates that the sample has no toxic action to cells. Cellular viabilities with different carriers of DOX−GdF_3:Yb^{3+}/Er^{3+}/Li^+ and DOX are also investigated. When the concentration is high, the cell viabilities of the two carriers are both lower (between 21% and 24%), which means that the system has high cell cytotoxicity when used as an anticancer drug. Furthermore, the cell viability is much different for DOX−GdF_3:Yb^{3+}/Er^{3+}/Li^+ and DOX when the concentration is lower. Obviously, the cell viability of GdF_3−DOX (67.8−86.2%) is much higher than that of DOX (22.7−71.9%), which is due to the different methods for the drug to enter the cells. When the concentration is low, DOX enters the cells by diffusion at a rapid rate. However, DOX−GdF_3:Yb^{3+}/Er^{3+}/Li^+ enters cells with a much lower rate, which is by endocytosis; the difference is inconspicuous with high concentration but evident with low concentration. In conclusion, a hollow GdF_3−DOX product inhibits proliferation of the cells well, which suggests its potential application for targeting cancer therapy.

CONCLUSIONS

In summary, uniform mesoporous GdF_3 hollow spheres have been successfully prepared by a facile synthesis method. The precursor $Gd(OH)CO_3$ spheres were first prepared through a classical coprecipitation process. Subsequently, uniform and size-tunable GdF_3 hollow spheres were easily coprecipitated with $NaBF_4$ at the sacrifice of the precursor at short reaction time and low temperature without using any surfactant and catalyst. Through regulation of the initial pH values and $NaBF_4$/Gd^{3+} molar ratios, the size, structure, and phase can be controllably tuned. Meanwhile, under 980 nm excitation, the UC emission colors of the as-prepared codoped GdF_3:Yb^{3+}/Er^{3+} hollow spheres were changed from green to yellow by a simple adjustment of the relative sensitizer ions' doping concentrations. Particularly, enhanced red emission was obtained only by doping 6% Li^+ in GdF_3:Yb^{3+}/Er^{3+}. GdF_3:Yb^{3+}/Ho^{3+} emitted strong green light when the concentration of Yb^{3+} is regulated at 15%. Furthermore, DOX release test and MTT cytotoxicity results demonstrated the potential application of hollow GdF_3 materials in the fields of drug-delivery system and targeted cancer therapy.

ASSOCIATED CONTENT

Supporting Information

TGA curve, FT-IR, and EDS of GdF_3 hollow spheres, CIE chromaticity diagram of GdF_3:*x*%Yb^{3+},1%Er^{3+} (*x* = 5, 20, 30, and 40), UC luminescent properties of GdF_3:15%Yb^{3+},1%Er^{3+},*y* %Li^+ (*y* = 0, 3, 6, 9, and 12), magnetization as a function of the applied field for GdF_3 hollow spheres, and illustration of phase and morphology for gadolinium fluorides with altered $NaBF_4$/Gd^{3+} molar ratios. This material is available free of charge via the Internet at http://pubs.acs.org.

AUTHOR INFORMATION

Corresponding Authors

*E-mail: gaishili@hrbeu.edu.cn.
*E-mail: yangpiaoping@hrbeu.edu.cn.

Notes

The authors declare no competing financial interest.

ACKNOWLEDGMENTS

Financial support from the National Natural Science Foundation of China (Grant 21271053), Research Fund for

the Doctoral Program of Higher Education of China (Grant 20112304110021), Natural Science Foundation of Heilongjiang Province (Grant LC2012C10), Program for New Century Excellent Talents in University, Harbin Sci.-Tech. Innovation Foundation (Grant RC2012XK017012), and the Fundamental Research Funds for the Central Universities of China (HEUCF20130910007) are gratefully acknowledged.

REFERENCES

(1) Xu, Z. H.; Ma, P. A.; Li, C. X.; Hou, Z. Y.; Zhai, X. F.; Huang, S. S.; Lin, J. *Biomaterials* **2011**, *32*, 4161−4173.
(2) Tang, H. Y.; Guo, J.; Sun, Y.; Chang, B. S.; Ren, Q. G.; Yang, W. L. *Int. J. Pharm.* **2011**, *421*, 388−394.
(3) Yang, P. P.; Gai, S. L.; Lin, J. *Chem. Soc. Rev.* **2012**, *41*, 3679−3698.
(4) Chen, H. M.; He, J. H.; Tang, H. M.; Yan, C. X. *Chem. Mater.* **2008**, *20*, 5894−5900.
(5) Jiao, Y. F.; Guo, J.; Shen, S.; Chang, B. S.; Zhang, Y. H.; Jiang, X. G.; Yang, W. L. *J. Mater. Chem.* **2012**, *22*, 17636−17643.
(6) Yan, E. F.; Fu, Y. L.; Wang, X. *J. Mater. Chem.* **2011**, *22*, 3147−3155.
(7) Tan, Y. W.; Bai, F.; Wang, D. S.; Peng, Q.; Wang, X.; Li, Y. D. *Chem. Mater.* **2007**, *19*, 5773−5778.
(8) Wang, Z. L.; Hao, J. H.; Chan, H. L. W.; Wong, W. T.; Wong, K. L. *Small* **2012**, *8*, 1863−1868.
(9) Wang, G. F.; Peng, Q.; Li, Y. D. *Acc. Chem. Res.* **2011**, *44*, 322−332.
(10) Chen, Y.; Yin, Q.; Ji, X. F.; Zhang, S. J.; Chen, H. R.; Zheng, Y. Y.; Sun, Y.; Qu, H. Y.; Wang, Z.; Li, Y. P.; Wang, X.; Zhang, K.; Zhang, L. L.; Shi, J. L. *Biomaterials* **2012**, *33*, 7126−7137.
(11) De Cock, L. J.; De Koker, S.; De Geest, B. G.; Grooten, J.; Vervaet, C.; Remon, J. P.; Sukhorukov, G. B.; Antipina, M. N. *Angew. Chem., Int. Ed.* **2010**, *49*, 6954−6973.
(12) Li, L.; Ding, J.; Xue, J. M. *Chem. Mater.* **2009**, *21*, 3629−3637.
(13) Jia, G.; Yang, M.; Song, Y. H.; You, H. P.; Zhang, H. J. *Cryst. Growth Des.* **2009**, *9*, 301−307.
(14) Alric, C.; Taleb, J.; Le Duc, G.; Mandon, C.; Billotey, C.; Le Meur-Herland, A.; Brochard, T.; Vocanson, F.; Janier, M.; Perriat, P.; Roux, S.; Tillement, O. *J. Am. Chem. Soc.* **2008**, *130*, 5908−5915.
(15) Bottrill, M.; Nicholas, L. K.; Long, N. J. *Chem. Soc. Rev.* **2006**, *35*, 557−571.
(16) Bridot, J.-L.; Faure, A.-C.; Laurent, S.; Riviere, C.; Billotey, C.; Hiba, B.; Janier, M.; Josserand, V.; Coll, J.-L.; Vander Elst, L.; Muller, R.; Roux, S.; Perriat, P.; Tillement, O. *J. Am. Chem. Soc.* **2007**, *129*, 5076−5084.
(17) Ju, Q.; Liu, Y. S.; Tu, D. T.; Zhu, H. M.; Li, R. F.; Chen, X. Y. *Chem.—Eur. J.* **2011**, *17*, 8549−8554.
(18) Signorini, M.; Bortolotti, F.; Poltronieri, L.; Bergamini, C. M. *Biol. Chem. Hoppe-Seyler* **1988**, *369*, 275−281.
(19) Kruger, R.; Braun, K.; Pipkorn, R.; Lehmann, W. D. *J. Anal. At. Spectrom.* **2004**, *19*, 852−857.
(20) Shokouhimehr, M.; Soehnlen, E. S.; Hao, J. H.; Griswold, M.; Flask, C.; Fan, X. D.; Basiljon, J. P.; Basu, S.; Huang, S. P. D. *J. Mater. Chem.* **2010**, *20*, 5251−5259.
(21) Jia, G.; Yang, M.; Song, Y. H.; You, H. P.; Zhang, H. J. *Cryst. Growth Des.* **2009**, *9*, 301−307.
(22) Xu, Z. P.; Zeng, Q. H.; Lu, G. Q.; Yu, A. B. *Chem. Eng. Sci.* **2006**, *61*, 1027−1040.
(23) Caravan, P. *Acc. Chem. Res.* **2009**, *42*, 851−862.
(24) Ju, Q.; Tu, D.; Liu, Y.; Li, R.; Zhu, H.; Chen, J.; Chen, Z.; Huang, M.; Chen, X. *J. Am. Chem. Soc.* **2012**, *134*, 1323−1330.
(25) Villaraza, A. J. L.; Bumb, A.; Brechbiel, M. W. *Chem. Rev.* **2010**, *110*, 2921−2959.
(26) Haase, M.; Schafer, H. *Angew. Chem., Int. Ed.* **2011**, *50*, 5808−5829.
(27) Kumar, R.; Nyk, M.; Ohulchanskyy, T. Y.; Flask, C. A.; Prasad, P. N. *Adv. Funct. Mater.* **2009**, *19*, 853−859.
(28) Li, C. X.; Lin, J. *J. Mater. Chem.* **2010**, *20*, 6831−6847.
(29) Li, Z.; Zhang, Y. *Angew. Chem., Int. Ed.* **2006**, *45*, 7732−7735.
(30) Mai, H. X.; Zhang, Y. W.; Si, R.; Yan, Z. G.; Sun, L. D.; You, L. P.; Yan, C. H. *J. Am. Chem. Soc.* **2006**, *128*, 6426−6436.
(31) Mai, H. X.; Zhang, Y. W.; Sun, L. D.; Yan, C. H. *J. Phys. Chem. C* **2007**, *111*, 13721−13729.
(32) Feng, Z. G.; Li, Y. S.; Niu, D. C.; Li, L.; Zhao, W. R.; Chen, H. R.; Li, L.; Gao, J. H.; Ruan, M. L.; Shi, J. L. *Chem. Commun.* **2008**, 2629−2631.
(33) Lin, Y. S.; Haynes, C. L. *Chem. Mater.* **2009**, *21*, 3979−3986.
(34) Tang, F. Q.; Li, L. L.; Chen, D. *Adv. Mater.* **2012**, *24*, 1504−1534.
(35) Tian, G.; Gu, Z. J.; Liu, X. X.; Zhou, L. J.; Yin, W. Y.; Yan, L.; Jin, S.; Ren, W. L.; Xing, G. M.; Li, S. J.; Zhao, Y. L. *J. Phys. Chem. C* **2011**, *115*, 23790−23796.
(36) He, X. D.; Ge, X. W. W.; Wang, M. Z.; Zhang, Z. C. *Polymer* **2005**, *46*, 7598−7604.
(37) Jia, G.; You, H. P.; Liu, K.; Zheng, Y. H.; Guo, N.; Zhang, H. J. *Langmuir* **2010**, *26*, 5122−5128.
(38) Song, Y. H.; You, H. P.; Huang, Y. J.; Yang, M.; Zheng, Y. H.; Zhang, L. H.; Guo, N. *Inorg. Chem.* **2010**, *49*, 11499−11504.
(39) Cheng, X. J.; Chen, M.; Wu, L. M.; Gu, G. X. *Langmuir* **2006**, *22*, 3858−3863.
(40) Khanal, A.; Inoue, Y.; Yada, M.; Nakashima, K. *J. Am. Chem. Soc.* **2007**, *129*, 1534−1535.
(41) Zhang, F.; Shi, Y. F.; Sun, X. H.; Zhao, D. Y.; Stucky, G. D. *Chem. Mater.* **2009**, *21*, 5237−5243.
(42) Zhang, L.; Yin, M.; You, H.; Yang, M.; Song, Y.; Huang, Y. *Inorg. Chem.* **2011**, *50*, 10608−10613.
(43) Kijkowska, R. *Thermochim. Acta* **2003**, *404*, 81−88.
(44) Liu, Y. C.; Yang, P. P.; Wang, W. X.; Dong, H. X.; Lin, J. *CrystEngComm* **2010**, *12*, 3717−3723.
(45) Di, W.; Ren, X.; Zhao, H.; Shirahata, N.; Sakka, Y.; Qin, W. *Biomaterials* **2011**, *32*, 7226−7233.
(46) Huang, S. H.; Xu, J.; Zhang, Z. G.; Zhang, X.; Wang, L. Z.; Gai, S. L.; He, F.; Niu, N.; Zhang, M. L.; Yang, P. P. *J. Mater. Chem.* **2012**, *22*, 16136−16144.
(47) Yin, Y. D.; Rioux, R. M.; Erdonmez, C. K.; Hughes, S.; Somorjai, G. A.; Alivisatos, A. P. *Science* **2004**, *304*, 711−714.
(48) Fan, H. J.; Knez, M.; Scholz, R.; Hesse, D.; Nielsch, K.; Zacharias, M.; Gosele, U. *Nano Lett.* **2007**, *7*, 993−997.
(49) Jia, L. P.; Zhang, Q.; Yan, B. *Mater. Res. Bull.* **2012**, *47*, 3301−3307.
(50) Liang, X.; Wang, X.; Zhuang, J.; Peng, Q.; Li, Y. D. *Adv. Funct. Mater.* **2007**, *17*, 2757−2765.
(51) Zhang, Q.; Yan, B. *Inorg. Chem.* **2010**, *49*, 6834−6839.
(52) Yang, D. M.; Li, C. X.; Li, G. G.; Shang, M. M.; Kang, X. J.; Lin, J. *J. Mater. Chem.* **2011**, *21*, 5923−5927.
(53) Yin, A. X.; Zhang, Y. W.; Sun, L. D.; Yan, C. H. *Nanoscale* **2010**, *2*, 953−959.
(54) Zhang, C. M.; Ma, P. A.; Li, C. X.; Li, G. G.; Huang, S. S.; Yang, D. M.; Shang, M. M.; Kang, X. J.; Lin, J. *J. Mater. Chem.* **2011**, *21*, 717−723.
(55) Li, Z. Q.; Zhang, Y.; Jiang, S. *Adv. Mater.* **2008**, *20*, 4765−4769.
(56) Zhang, Q.; Yan, B. *Chem. Commun.* **2011**, *47*, 5867−5869.
(57) Li, C. X.; Quan, Z. W.; Yang, P. P.; Huang, S. S.; Lian, H. Z.; Lin, J. *J. Phys. Chem. C* **2008**, *112*, 13395−13404.
(58) Liu, R.; Tu, D.; Liu, Y.; Zhu, H.; Li, R.; Zheng, W.; Ma, E.; Chen, X. *Nanoscale* **2012**, *4*, 4485−4491.
(59) Liu, X. H.; Wang, L. M.; Wang, Z. Y.; Li, Z. Q. *J. Mater. Res.* **2011**, *26*, 82−87.
(60) Zeng, J. H.; Li, Z. H.; Su, J.; Wang, L. Y.; Yan, R. O.; Li, Y. D. *Nanotechnology* **2006**, *17*, 3549−3555.
(61) Zeng, S. J.; Tsang, M. K.; Chan, C. F.; Wong, K. L.; Fei, B.; Hao, J. H. *Nanoscale* **2012**, *4*, 5118−5124.
(62) Pollnau, M.; Gamelin, D. R.; Lüthi, S. R.; Güdel, H. U.; Hehlen, M. P. *Phys. Rev. B* **2000**, *61*, 3337−3346.
(63) Wang, H. Q.; Nann, T. *ACS Nano* **2009**, *3*, 3804−3808.

(64) Yin, W. Y.; Zhao, L. N.; Zhou, L. J.; Gu, Z. J.; Liu, X. X.; Tian, G.; Jin, S.; Yan, L.; Ren, W. L.; Xing, G. M.; Zhao, Y. L. *Chem.—Eur. J.* **2012**, *18*, 9239−9245.
(65) He, M.; Huang, P.; Zhang, C. L.; Hu, H. Y.; Bao, C. C.; Gao, G.; He, R.; Cui, D. X. *Adv. Funct. Mater.* **2011**, *21*, 4470−4477.
(66) Wang, G.; Peng, Q.; Li, Y. *Chem.—Eur. J.* **2010**, *16*, 4923−4931.
(67) Wu, Y.; Li, C.; Yang, D.; Lin, J. *J. Colloid Interface Sci.* **2011**, *354*, 429−435.
(68) Dong, C. H.; Raudsepp, M.; van Veggel, F. *J. Phys. Chem. C* **2009**, *113*, 472−478.
(69) Yi, G. S.; Chow, G. M. *J. Mater. Chem.* **2005**, *15*, 4460−4464.
(70) Cheng, Q.; Sui, J.; Cai, W. *Nanoscale* **2012**, *4*, 779−784.
(71) Zeng, S.; Xiao, J.; Yang, Q.; Hao, J. *J. Mater. Chem.* **2012**, *22*, 9870−9874.
(72) Dai, Y. L.; Ma, P. A.; Cheng, Z. Y.; Kang, X. J.; Zhang, X.; Hou, Z. Y.; Li, C. X.; Yang, D. M.; Zhai, X. F.; Lin, J. *ACS Nano* **2012**, *6*, 3327−3338.
(73) Park, Y. I.; Kim, H. M.; Kim, J. H.; Moon, K. C.; Yoo, B.; Lee, K. T.; Lee, N.; Choi, Y.; Park, W.; Ling, D.; Na, K.; Moon, W. K.; Choi, S. H.; Park, H. S.; Yoon, S.-Y.; Suh, Y. D.; Lee, S. H.; Hyeon, T. *Adv. Mater.* **2012**, *24*, 5755−5761.
(74) Wang, L.; Xing, H.; Zhang, S.; Ren, Q.; Pan, L.; Zhang, K.; Bu, W.; Zheng, X.; Zhou, L.; Peng, W.; Hua, Y.; Shi, J. *Biomaterials* **2013**, *34*, 3390−3401.